lubricants

MDPI

Article

Film Thickness Prediction from Dichromatic Interference Images Based on Dual-Wavelength Physics-Guided Graph Neural Network

Peng Yue [1], Jiaqing Wang [1,2], Zhimin Shi [1,2], Chen He [1,2], Xiaoran Zhu [1,*] and Yujuan Zhang [3,*]

[1] School of Mechanical Engineering, Yellow River Conservancy Technical University, Kaifeng 475003, China; ypzzu@163.com (P.Y.); wang_jiaqing2026@163.com (J.W.); shi_zhimin2026@163.com (Z.S.); he_chen2026@163.com (C.H.)
[2] School of Mechanical Engineering, North China University of Water Resources and Electric Power, Zhengzhou 450046, China
[3] National & Local Joint Engineering Research Center for Applied Technology of Hybrid Nanomaterials, Henan University, Kaifeng 475004, China
* Correspondence: xiaoran.zhu@foxmail.com (X.Z.); cnzhangyujuan@henu.edu.cn (Y.Z.)

Abstract

Dichromatic optical interferometry provides rich optical information for lubricant film-thickness measurement. However, experimental data are typically limited to a small number of discrete operating conditions, making it difficult to learn the nonlinear relationship among entrainment speed, dichromatic interference images, and lubricant film thickness. To address this limitation, a Dual-Wavelength Physics-Guided Graph Neural Network (DW-PG-GNN) is proposed for intermediate lubrication-state characterization from sparse experimental observations. Rather than directly regressing film thickness from interference images, the proposed framework learns the nonlinear relationship among entrainment speed, dichromatic interference images, and lubricant film thickness through a unified physics-guided learning framework. Specifically, graph representations capture the structural continuity and cross-wavelength coupling characteristics of dichromatic interference fringes, while a physics-guided residual learning strategy embeds analytical film-thickness priors from classical elastohydrodynamic lubrication (EHL) theory into an implicit neural representation for intermediate state prediction. A differentiable interference renderer further constrains the consistency between predicted film thickness and reconstructed dichromatic interference images, ensuring optical and physical consistency throughout the learning process. Validation based on sparse experimental datasets acquired from a ball-on-disc EHL rig demonstrates reliable average film-thickness prediction and interference-image reconstruction under the investigated operating conditions. The prediction errors remain within 2.2% for trained conditions and 8.67% for unseen entrainment-speed interpolation conditions.

Keywords: dichromatic optical interferometry; graph neural network; physics-guided learning; film thickness prediction; implicit neural representation

Check for updates

Received: 19 July 2026
Revised: 13 August 2026
Accepted: 19 August 2026
Published: 21 August 2026

Copyright: © 2026 by the authors. Licensee MDPI, Basel, Switzerland. This article is an open access article distributed under the terms and conditions of the Creative Commons Attribution (CC BY) license.

1. Introduction

Friction and wear are among the primary factors contributing to the failure of high-end mechanical systems, such as gears, bearings, and hydraulic components, and have long attracted significant attention in studies of mechanical reliability and service life. For these critical tribological contacts, the service life and reliability largely depend on the

formation and maintenance of an effective lubricant film, which is primarily governed by elastohydrodynamic lubrication (EHL) [1–3]. Under EHL conditions, lubricant film formation is governed by the coupled effects of hydrodynamic pressure, elastic deformation, and lubricant rheology [1,2]. As a critical indicator of lubrication performance, film thickness directly reflects the load-carrying capability and lubrication state of tribological contacts [3,4]. Therefore, accurate characterization of lubricant film thickness remains an important topic in tribology and lubrication engineering.

To obtain film-thickness information within lubricated contacts, various measurement techniques have been developed, including ultrasonic methods, electrical methods, and optical interferometry [5–8], among which optical interferometry has become one of the most widely adopted approaches for EHL film-thickness characterization due to its non-contact measurement capability, high spatial resolution, and full-field observation ability [5,9]. Among optical approaches, dichromatic interferometry effectively resolves the fringe-order ambiguity associated with conventional monochromatic interferometry by incorporating interference information from multiple wavelengths, thereby significantly extending the measurable film-thickness range [10,11]. In this work, following established practice in EHL interferometry [11], a 532 nm green laser and a 650 nm red laser are employed, with their interference signals directly recorded by the corresponding green and red channels of a standard RGB camera. This configuration ensures efficient spectral separation while maintaining compatibility with conventional color imaging systems, enabling stable acquisition of dichromatic interference patterns [11]. Beyond film-thickness measurement, dichromatic interference images also contain abundant optical and physical information related to lubricant-film morphology, elastic deformation, and lubrication-state evolution [11–13]. Consequently, these images can be regarded not only as measurement outcomes but also as rich physical representations of EHL states. Nevertheless, acquiring high-quality dichromatic interference images still requires complex experimental setups, rigorous calibration procedures, and substantial post-processing efforts [11,14]. Moreover, due to limitations in experimental cost, measurement efficiency, and equipment stability, experimental observations are generally available only at a finite number of discrete operating conditions, whereas lubrication states evolve continuously with changing operating parameters [9,14]. Consequently, it remains difficult to directly characterize intermediate lubrication states from experimental observations alone.

In practical EHL systems, variations in operating conditions continuously alter the pressure distribution, lubricant flow, and film-thickness profile within the contact region, leading to corresponding changes in interference-image characteristics [1,3]. As a result, lubrication-state evolution can be viewed as a continuous nonlinear process linking operating conditions, optical responses, and physical lubrication parameters. Although conventional interpolation or empirical fitting methods can be employed to estimate intermediate states, such approaches often fail to capture the underlying physical evolution, particularly under sparse sampling conditions [15]. Therefore, there is a need for data-driven approaches capable of learning the relationship between operating conditions, interference images, and representative film-thickness parameters from limited experimental observations [15].

In recent years, machine learning and deep learning techniques have been increasingly applied to EHL and tribology problems. Supervised learning methods, including regression models and convolutional neural networks, have been used to predict scalar film-thickness values from optical or numerical data [16]. Surrogate modeling approaches have been proposed to approximate simulation outputs, and neural networks have been employed to estimate lubrication parameters from limited experimental datasets [15,17]. While these methods demonstrate the potential of data-driven modeling, most studies have focused

on either point-wise thickness prediction or mapping from simulation data rather than experimental interference images [17,18]. Moreover, few studies have attempted to model the continuous evolution of interference patterns or to capture the sequential relationship among operating conditions, optical responses, and film-thickness characteristics under small-sample constraints [19]. Therefore, relatively few studies have explored learning the relationship between operating conditions and dichromatic interference images under sparse experimental conditions.

Motivated by the above challenges, this study investigates the relationship between entrainment velocity, dichromatic interference images, and average lubricant film thickness under physically constrained EHL operating conditions. A physics-guided deep-learning framework is proposed to investigate this relationship by establishing a sequential mapping from entrainment velocity to dichromatic interference-image evolution and subsequently to the corresponding average lubricant film thickness. The proposed framework provides a data-driven approach for characterizing the relationship between operating conditions, interference-image evolution, and representative film-thickness parameters using sparse experimental observations.

2. Theoretical Background

2.1. Graph-Based Implicit Neural Representation

To capture non-Euclidean spatial features from discrete dual-wavelength fringe patterns and map them to continuous domains, Graph Convolutional Network (GCN) [20] and Sinusoidal Representation Network (SIREN) [21] are integrated. First, for a graph with adjacency matrix A, GCN aggregates spatial and topological neighbor features through spectral convolution [18]:

$$H^{(l+1)} = \sigma\left(\widetilde{D}^{-\frac{1}{2}}\widetilde{A}\widetilde{D}^{-\frac{1}{2}}H^{(l)}W^{(l)}\right), \tag{1}$$

where $H^{(l)}$ is the node feature matrix of the l-th layer; $W^{(l)}$ is the weight matrix; $\sigma(\cdot)$ denotes the nonlinear transformation function after graph convolution. In the proposed framework, the Gaussian Error Linear Unit (GELU) activation is employed to introduce nonlinear feature transformation during graph feature propagation; $\widetilde{A} = A + I_N$ (I_N is the identity matrix); and $\widetilde{D}$ is the diagonal degree matrix with elements $\widetilde{D}_{ii} = \sum_j \widetilde{A}_{ij}$.

Subsequently, to resolve the spectral bias of standard activation functions in high-frequency coordinate mapping, SIREN employs periodic sine waves to represent continuous fields [21]:

$$x^{(l+1)} = \sin\left(\omega_0\left(W^{(l)}x^{(l)} + b^{(l)}\right)\right), \tag{2}$$

where $x^{(l)}$ and $x^{(l+1)}$ represent the input and output vectors of the l-th layer, respectively; $W^{(l)}$ and $b^{(l)}$ are the weights and biases; and ω_0 represents the frequency scaling factor controlling the bandwidth of the sinusoidal representation. In the proposed ResSIREN module, ω_0 is predefined as 5.0 and remains fixed during optimization, while the network weights and biases are updated through the training process. This fixed frequency factor enables the implicit representation to capture continuous variations in lubricant film thickness with respect to spatial coordinates and operating conditions.

2.2. Physics-Guided Deep Learning Paradigm

Physics-guided deep learning integrates prior physical laws or analytical formulations into neural network training to ensure physical consistency and improve generalization under sparse observations [22,23]. In general, the integration of physical knowledge is established at two fundamental levels:

First, at the architectural level, an analytical physical prior $f_{phy}(z)$ is coupled with a neural network $f_\theta(x)$ in a hybrid or residual structure to predict a target physical state y [22]:

$$y = f_{\text{phy}}(z) + f_\theta(x), \tag{3}$$

Second, at the optimization level, the network training is regularized by incorporating physical governing laws, spatial gradients, or boundary constraints directly into a multi-objective loss function [22]:

$$\mathcal{L}_{\text{total}} = w_{\text{data}}\mathcal{L}_{\text{data}} + w_{\text{phys}}\mathcal{L}_{\text{phys}}, \tag{4}$$

where $\mathcal{L}_{\text{data}}$ is the standard data-driven discrepancy; $\mathcal{L}_{\text{phys}}$ penalizes violations of physical principles; and w_{data}, w_{phys} are task-specific loss weights.

2.3. Thin-Film Dichromatic Optical Interferometry

Thin-film dichromatic optical interferometry resolves sub-micron film thicknesses from dual-wavelength fringe patterns [10]. Incorporating the boundary phase shift and spectral coherence decay under a finite source bandwidth, the rendered light intensity $I(\lambda)$ is modeled as [24]:

$$I(\lambda) = A_\lambda + B_\lambda \cdot \gamma \cdot \cos\left(\frac{4\pi \cdot OPL}{\lambda} + \Delta\phi\right), \tag{5}$$

$$\gamma = \exp\left(-\left(\frac{\pi \cdot \Delta\lambda \cdot 2OPL}{\lambda^2\sqrt{\ln 2}}\right)^2\right), \tag{6}$$

$$OPL = n_{oil} \cdot h + n_{spacer} \cdot h_{spacer}, \tag{7}$$

where A_λ and B_λ are the background intensity and fringe contrast; γ is the coherence decay factor; $\Delta\phi$ is the boundary phase shift; $\Delta\lambda$ is the light source full-width at half-maximum; OPL is the single-pass optical path length of the layered media [25]; n_{oil} and n_{spacer} are the refractive indices; h is the local film thickness; and h_{spacer} is the spacer thickness. For the optical configuration considered in this study, the spacer layer is a diamond-like carbon (DLC) layer with a fixed thickness of 120.0 nm and a refractive index of 2.0. These parameters are regarded as known optical constants in the interference model and are kept fixed during model optimization.

3. Dual-Wavelength Physics-Guided Graph Neural Network (DW-PG-GNN)

The evolution of EHL states is inherently continuous, whereas experimental observations can only be obtained under a limited number of discrete operating conditions. Consequently, conventional data-driven approaches that directly establish mappings between interference images and lubricant film thickness are unable to accurately characterize unseen intermediate lubrication states. To overcome this limitation, a DW-PG-GNN is developed by integrating graph representation learning, coordinate-based implicit neural representation, and physics-guided optimization into a unified learning framework. Based on sparse dual-wavelength interference observations, the proposed framework establishes a physically consistent mapping among operating conditions, interference images, and lubricant film thickness, thereby enabling intermediate lubrication-state reconstruction and lubricant film thickness prediction under independent validation operating conditions.

3.1. DW-PG-GNN

Figure 1 illustrates the overall architecture of the proposed DW-PG-GNN framework. The network consists of three major components: the Feature Extraction & Graph Represen-

tation module, the Physics-guided Thickness–Renderer module, and the Multi-objective Physics-guided Loss module.

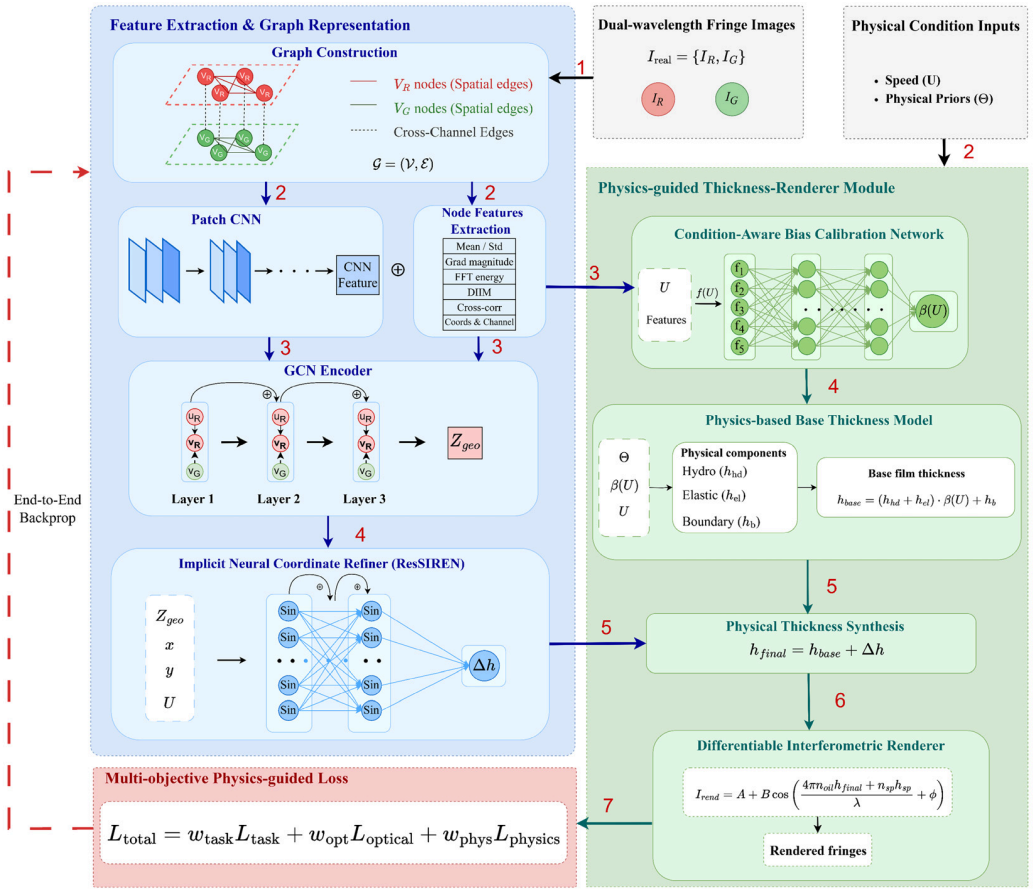


Figure 1. The structure of the DW-PG-GNN model.

Feature Extraction & Graph Representation Module: The experimentally acquired dichromatic interference images $I_{real} = \{I_R + I_G\}$ are first preprocessed and subsequently input into the Feature Extraction & Graph Representation module. Compared with single-wavelength observations, the dual-wavelength interference images preserve complementary optical responses from the red and green wavelengths, providing more comprehensive physical information for characterizing lubricant film characteristics. To effectively exploit this complementary information, each interference image is partitioned into multiple non-overlapping 16×16 local patches, which are subsequently mapped into graph nodes. Each patch from the red and green channels is treated as an individual node while preserving the spatial correspondence between the two wavelength responses. Unlike conventional graph representations constructed solely from image appearance, spatial adjacency edges are established according to a 4-connected neighborhood criterion, where neighboring patches within the same wavelength channel are connected and self-loops are introduced to retain each node's original representation during graph convolution. Meanwhile, cross-wavelength connection edges are established between nodes with identical spatial locations in the two wavelength channels. Since the two wavelength-dependent interference responses originate from the same lubricant film state, these cross-wavelength connections enable the exchange of complementary optical information between corresponding nodes, resulting in a dual-wavelength graph representation. Based on the constructed graph, the Node Feature Extraction module computes a 16-dimensional physical attribute vector for each node, including intensity statistics, gradient information, frequency-domain charac-

teristics, dichromatic intensity relationships, and spatial position information, while the Patch CNN extracts latent local texture and color variation features. These complementary features are subsequently propagated through the GCN Encoder, where neighborhood information is aggregated by graph convolution to generate the shared geometric representation Z_{geo}. By jointly exploiting the complementary optical information of the dual wavelengths together with the topological relationships of interference fringes, this module provides a unified and physically meaningful geometric representation for subsequent intermediate lubrication-state learning. Subsequently, the shared geometric representation Z_{geo}, together with the entrainment speed U and the spatial coordinates (x, y), is fed into the implicit neural coordinate refinement network (ResSIREN), which treats the entrainment speed as a continuous coordinate variable and learns the residual film thickness Δh to compensate for the nonlinear lubrication characteristics that cannot be accurately captured by the analytical model.

Physics-guided Thickness–Renderer Module: The operating parameter (U, θ) corresponding to $I_{real} = \{I_R + I_G\}$ are fed into the Bias Calibration Network to learn the calibration coefficient $\beta(U)$ under different operating conditions. Rather than directly predicting lubricant film thickness from experimental data alone, the proposed framework introduces a physics-based prior derived from classical EHL theory. Specifically, the analytical base film thickness h_{base} is calculated using the Hamrock–Dowson film-thickness correlation with the corresponding operating parameters. Since ideal EHL correlations cannot fully capture deviations caused by practical lubricant properties and experimental conditions, the learned calibration coefficient $\beta(U)$ is employed to calibrate the theoretical film-thickness estimation under the corresponding operating conditions. The resulting calibrated thickness provides a corrected physical prior for subsequent residual refinement. The coefficient is optimized jointly with the entire framework through the proposed multi-objective loss function to adapt the theoretical prior to experimental observations. Subsequently, the analytical base film thickness h_{base} and the residual film thickness Δh are combined to obtain the final predicted film thickness h_{final}. Instead of using the predicted thickness only for numerical supervision, the predicted film thickness is further fed into the Differentiable Interferometric Renderer to reconstruct the corresponding dichromatic interference image according to the optical interference principle. By establishing the physical correspondence between lubricant film thickness and optical interference responses, the reconstructed image provides an additional physics-guided constraint for network optimization. Through the collaborative learning of analytical modeling, nonlinear residual refinement, and differentiable optical rendering, this module establishes a physically consistent interpolation mapping from operating conditions to lubricant film thickness and dual-wavelength interference responses.

Multi-objective Physics-guided Loss Module: Finally, the outputs generated by the previous two modules are jointly delivered to the Multi-objective Physics-guided Loss module for end-to-end optimization. To ensure that the reconstructed lubrication states are not only consistent with the experimental observations but also satisfy the underlying physical principles of EHL, multiple supervisory signals are jointly incorporated into the network optimization. Specifically, the task loss L_{task} supervises the lubricant film thickness prediction, enabling the network to learn the mapping between interference images, operating conditions, and film-thickness characteristics. The optical consistency loss $L_{optical}$ constrains the reconstructed interference image to remain consistent with the experimentally observed image, thereby preserving the physical correspondence between lubricant film thickness and optical interference responses. The physics consistency loss $L_{physics}$ further regularizes the prediction according to the analytical film-thickness prior. Specifically, the thickness anchor constraint is employed to anchor the analytical prior to experimental measurements,

while additional regularization terms are incorporated to maintain physically reasonable thickness variations during intermediate state reconstruction. By jointly optimizing these complementary objectives, the proposed frame-work enables graph representation learning, coordinate-based implicit representation, and physics-guided lubricant film thickness prediction to be collaboratively optimized in a unified end-to-end manner.

3.2. DW-PG-GNN-Based Film Thickness Prediction and Reconstruction Method

Based on the proposed DW-PG-GNN, a complete workflow for lubricant film thickness prediction and dichromatic interference image reconstruction is established. As illustrated in Figure 2, the proposed method consists of four successive stages, namely the Data Preparing Stage, Training Stage, Prediction Stage, and Inversion Stage.

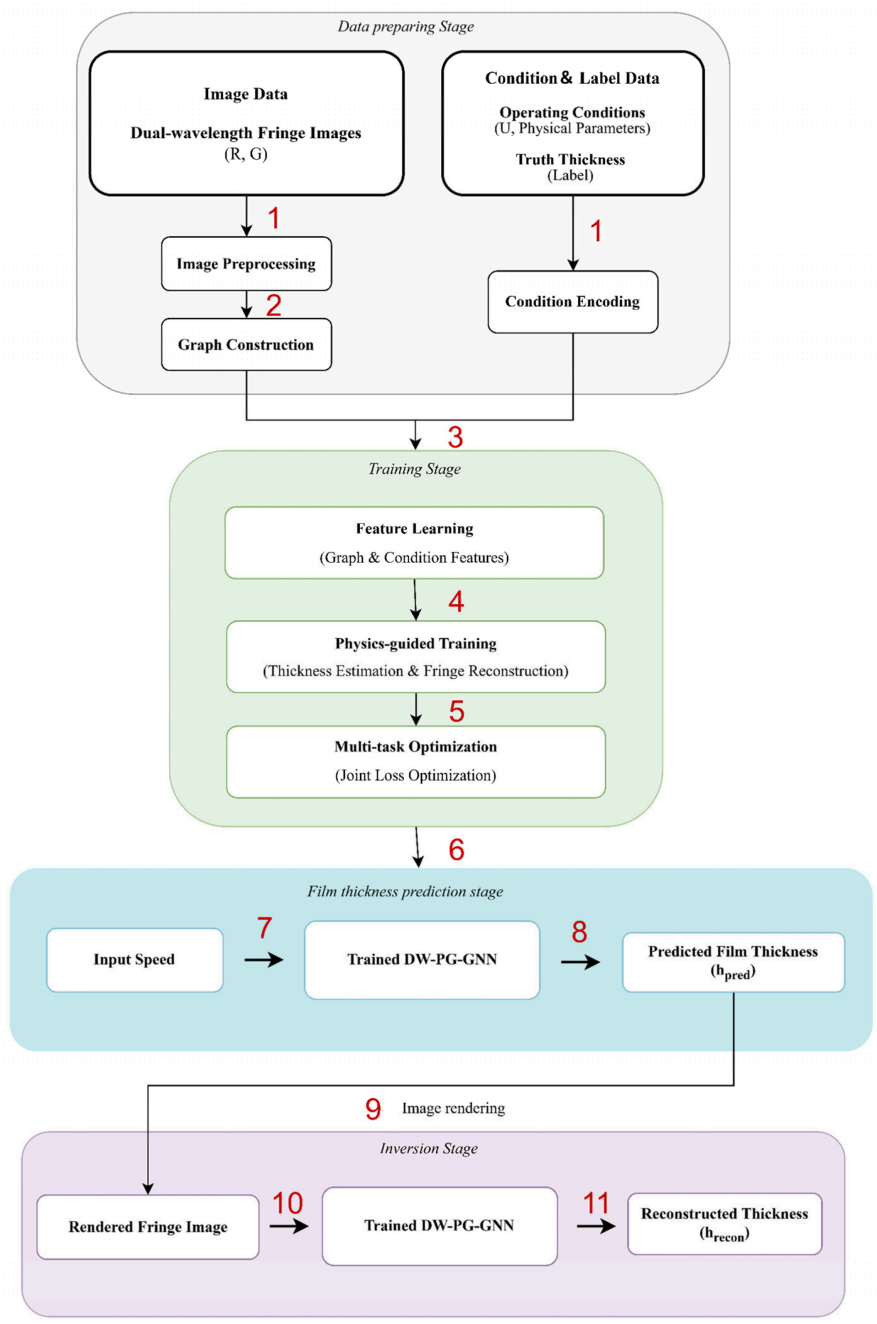


Figure 2. Flowchart of the proposed DW-PG-GNN-based continuous lubrication-state learning method.

The experimentally acquired dichromatic interference images are first preprocessed through contact-region alignment, contrast enhancement, and noise suppression to improve the quality and consistency of the input data. Subsequently, the processed images are transformed into graph representations, while the corresponding operating conditions and ground-truth lubricant film thicknesses are encoded as condition vectors, providing unified input information for subsequent network learning.

The graph representations together with the encoded condition information are fed into the proposed DW-PG-GNN for feature learning and physics-guided training. The network predicts the lubricant film thickness under the given operating conditions and reconstructs the corresponding dichromatic interference image using the Differentiable Interferometric Renderer. During training, the network parameters are iteratively optimized by jointly minimizing the discrepancy between the reconstructed interference image and the experimentally observed image, together with the lubricant film thickness prediction error, enabling data-driven learning and physical constraints to be collaboratively incorporated into the optimization process.

After the network has been trained, the proposed DW-PG-GNN directly predicts the corresponding lubricant film thickness, denoted as h_{pred}, for an arbitrary entrainment speed within the learned operating range. The predicted lubricant film thickness is subsequently converted into the corresponding dichromatic interference image through the Differentiable Interferometric Renderer. The predicted lubricant film thickness is further compared with the experimental measurement to evaluate the prediction accuracy and generalization capability of the proposed method under independent validation operating conditions.

To further demonstrate the inversion capability of the proposed framework, the rendered dichromatic interference image generated from the predicted lubricant film thickness is re-input into the trained DW-PG-GNN to obtain a reconstructed lubricant film thickness, denoted as h_{recon}. By comparing h_{pred} with h_{recon}, the consistency between the forward prediction and inverse reconstruction processes is evaluated, thereby validating the physical consistency and closed-loop reconstruction capability of the proposed framework.

4. Experiments, Results and Discussions

4.1. Experimental Platform

To acquire dichromatic interference images under EHL conditions, experiments were conducted using a ball-on-disc EHL test rig based on the principle of dichromatic optical interferometry, as shown in Figure 3. The experimental apparatus mainly consists of a ball-on-disc contact module, a driving system, a loading mechanism, and a lubricant supply system, enabling stable ball-on-disc EHL experiments and reliable acquisition of dichromatic interference images.

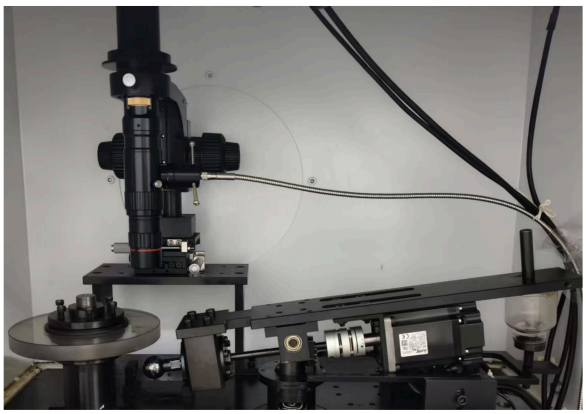
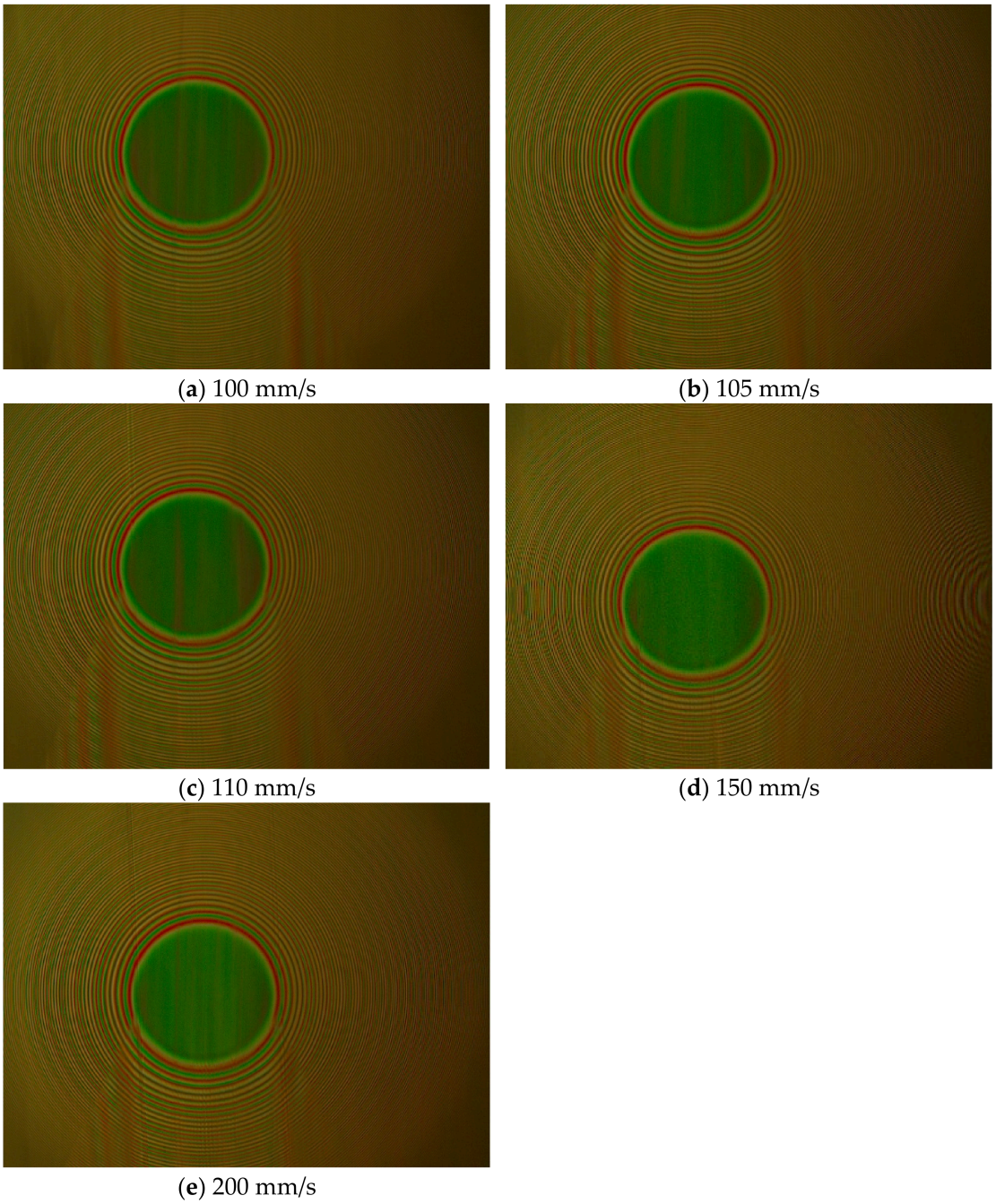


Figure 3. Ball-on-disc EHL experimental setup.

Using the experimental apparatus, ball-on-disc EHL experiments were conducted at five discrete entrainment speeds of 100, 105, 110, 150, and 200 mm/s. The entrainment speed was selected as the only varying operating parameter, while the applied normal load, lubricant type (PAO4 with 1.0% DNS), ambient temperature, and material properties of the contact pair remained unchanged. Representative dichromatic RGB interference images acquired at different entrainment speeds are shown in Figure 4, and the corresponding average lubricant film thickness along the contact diameter was extracted from the interference images through numerical analysis and used as the representative film-thickness parameter in this study. The selection of average film thickness is consistent with the objective of characterizing the relationship between entrainment-speed-induced interference-image evolution and representative lubrication-state variation under controlled EHL conditions. The operating conditions and corresponding film thicknesses are summarized in Table 1.



(**a**) 100 mm/s (**b**) 105 mm/s

(**c**) 110 mm/s (**d**) 150 mm/s

(**e**) 200 mm/s

Figure 4. Representative dichromatic interference images at different entrainment speeds.

Table 1. Experimental conditions and corresponding average lubricant film thicknesses.

Lubricant	DNS (%)	Speed (mm/s)	Average Film Thickness (nm)
PAO4	1.0%DNS	100	35
PAO4	1.0%DNS	105	27
PAO4	1.0%DNS	110	18
PAO4	1.0%DNS	150	23
PAO4	1.0%DNS	200	20

It can be observed from Table 1 that the measured average film thickness does not strictly follow the monotonic increasing trend predicted by classical isothermal EHL theory. This difference may be associated with the specific lubricant formulation used in this study. The employed lubricant (PAO4 with 1.0% DNS polar additive) may introduce additional interfacial contributions to the measured film thickness, indicating that the obtained value represents the combined effects of hydrodynamic film formation and lubricant–surface interactions rather than a purely hydrodynamic EHL film thickness. Under such additive-containing lubrication conditions, variations in entrainment speed may influence both hydrodynamic film formation and lubricant–surface interactions, resulting in a non-monotonic evolution of the measured film thickness within the investigated speed range. Therefore, the observed variation should be understood as the combined response of the specific lubricant system rather than evaluated solely according to the classical velocity-dependent EHL scaling relationship.

4.2. Film Thickness Prediction Under Different Operating Conditions

Building upon the experimental dataset established in Section 4.1, the proposed model is trained using interference images collected under three discrete entrainment-speed conditions, while two additional independent validation conditions are introduced to evaluate its capability of predicting unseen intermediate lubrication states between discrete experimental conditions.

As summarized in Table 2, the training dataset consists of interference images collected at 100, 150, and 200 mm/s, corresponding to different lubricant film thickness states. Two additional conditions (105 and 110 mm/s) are not involved in model training and are used as independent validation conditions for evaluating the model's prediction performance under the same lubricant, loading, temperature, and material conditions.

Table 2. Training dataset composition for film thickness prediction.

Speed (mm/s)	Sample Numbers	Label (Thickness/nm)
100	22	35
150	17	23
200	12	20

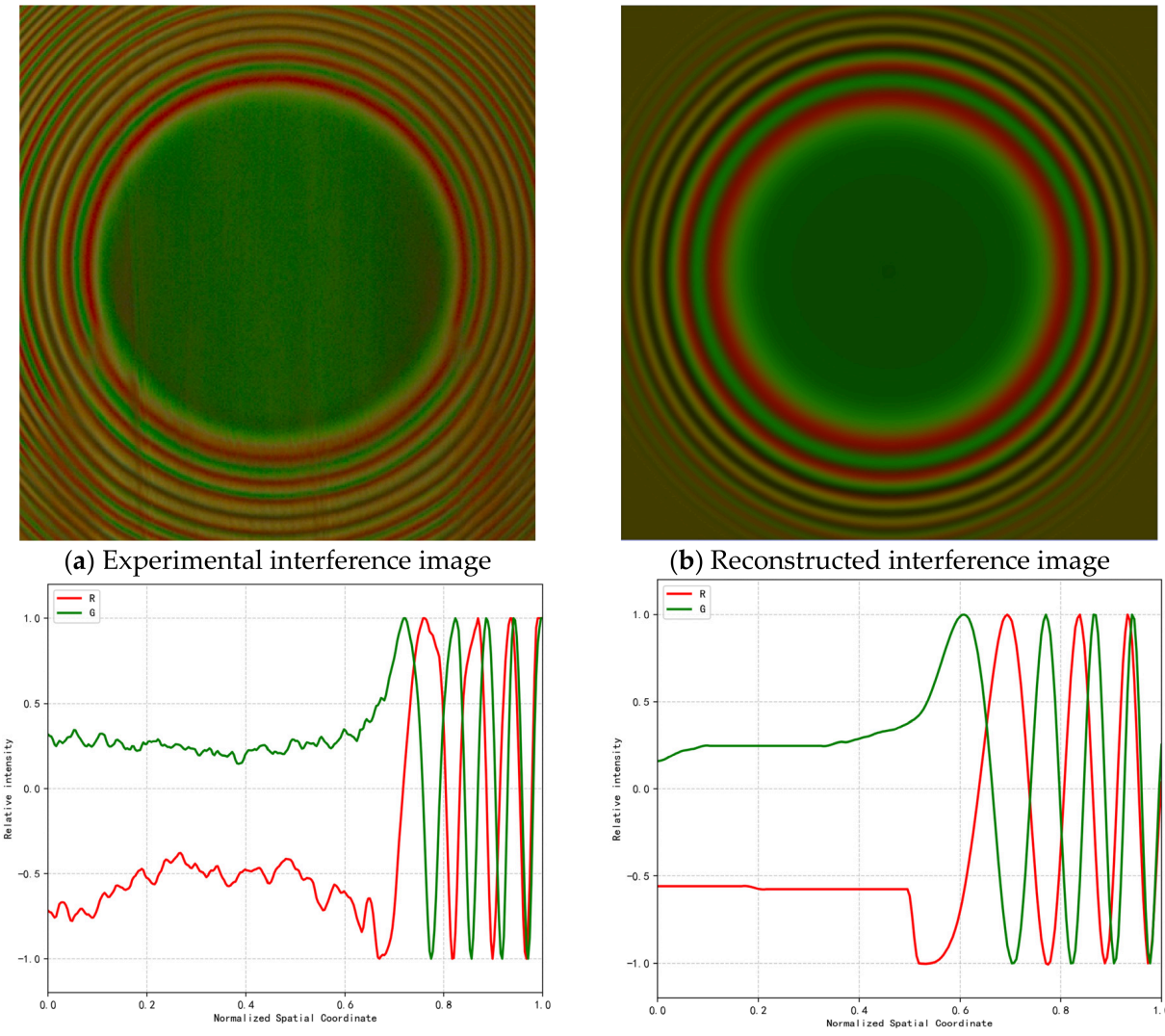
After model training, the proposed framework was applied to predict lubricant film thickness under different operating conditions. Table 3 summarizes the comparison between the predicted thickness values and experimental measurements. For the known operating conditions (100, 150, and 200 mm/s), the prediction errors remain below 2.20%. For the independent validation conditions (105 and 110 mm/s), the prediction errors are maintained within 9%.

Table 3. Comparison between predicted and measured film thickness.

Speed (mm/s)	Training Coverage	Measured (nm)	h_{pred} (nm)	Prediction Error (%)
100	Included	35	35.77	2.20
150	Included	23	23.30	1.30
200	Included	20	20.20	1.00
105	Excluded	27	25.49	5.59
110	Excluded	18	19.56	8.67

4.3. Interference Pattern Reconstruction

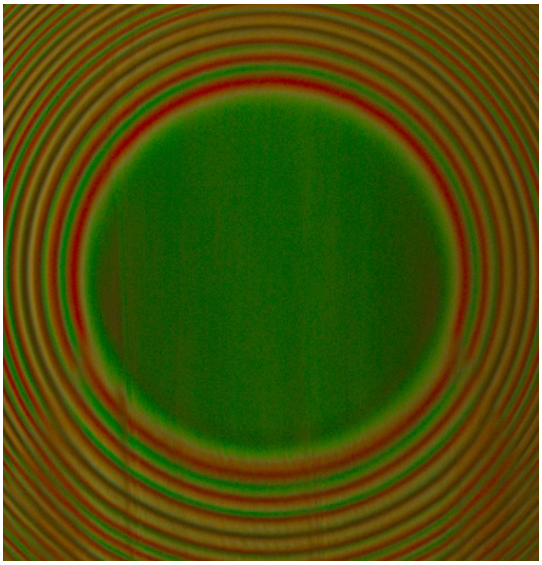
Based on the predicted film thickness obtained from the proposed framework, the corresponding dichromatic interference images were reconstructed through forward rendering using the optical model. As shown in Figures 5–9, the reconstructed interference images preserve the main fringe structures, radial distribution characteristics, and color variation trends observed in the experimental images. The reconstruction results are qualitatively examined based on the consistency of these principal optical features.



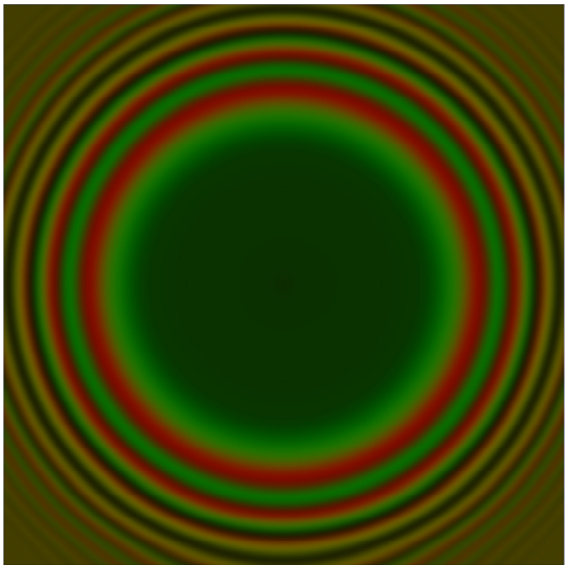
(**a**) Experimental interference image (**b**) Reconstructed interference image

(**c**) R/G intensity profile of experimental image (**d**) R/G intensity profile of reconstructed image

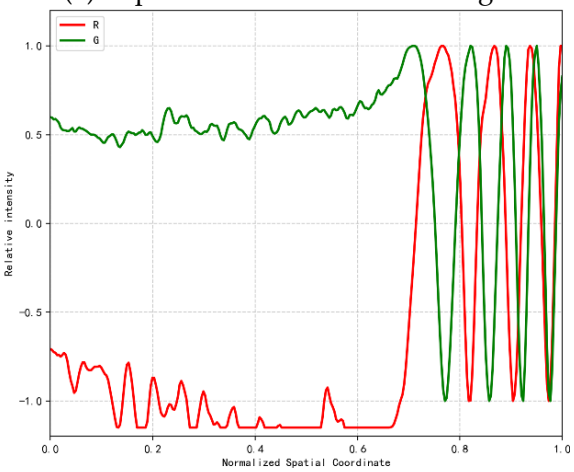
Figure 5. Interference response reconstruction at 100 mm/s operating condition.



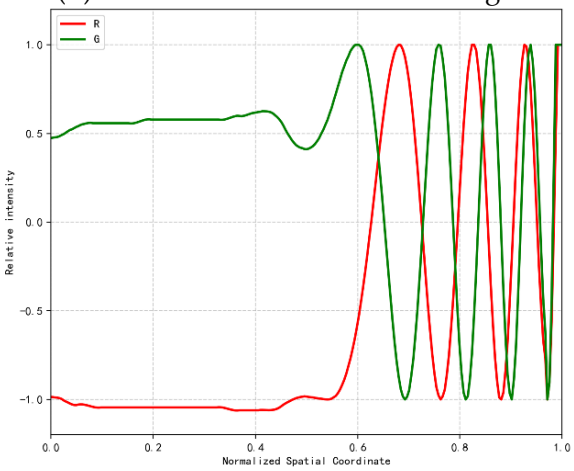
(**a**) Experimental interference image



(**b**) Reconstructed interference image

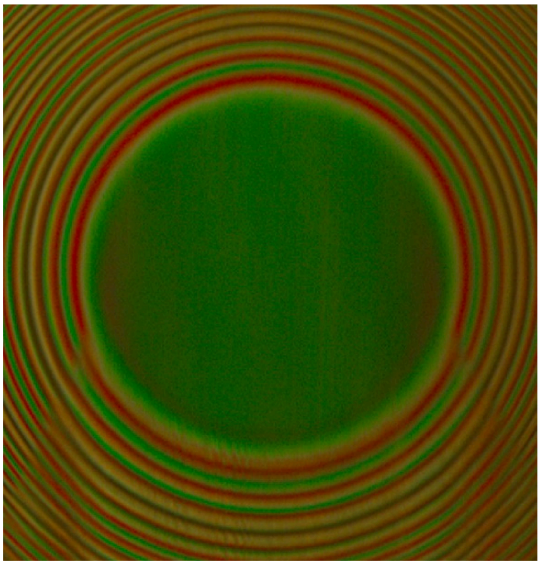


(**c**) R/G intensity profile of experimental image

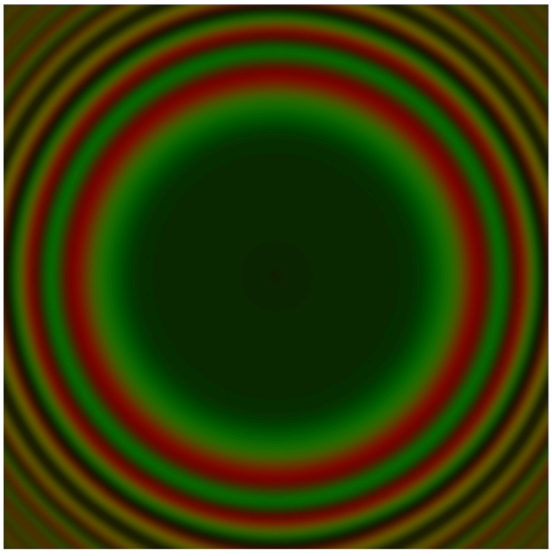


(**d**) R/G intensity profile of reconstructed image

Figure 6. Interference response reconstruction at 150 mm/s operating condition.

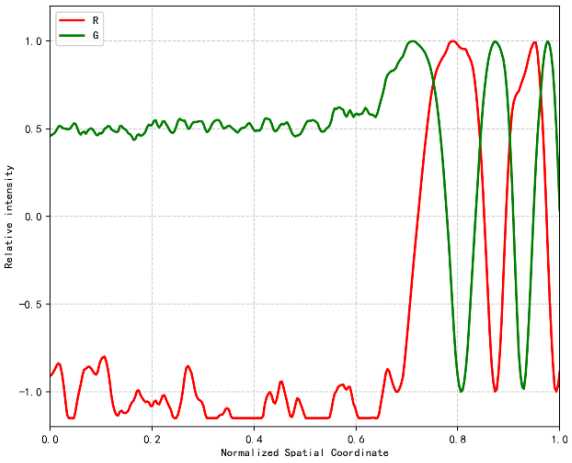


(**a**) Experimental interference image

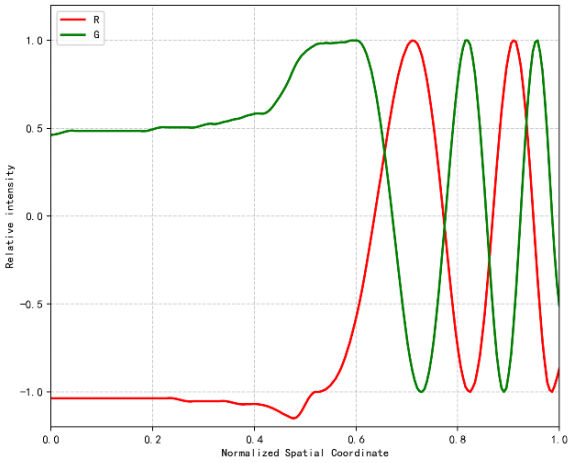


(**b**) Reconstructed interference image

Figure 7. *Cont.*

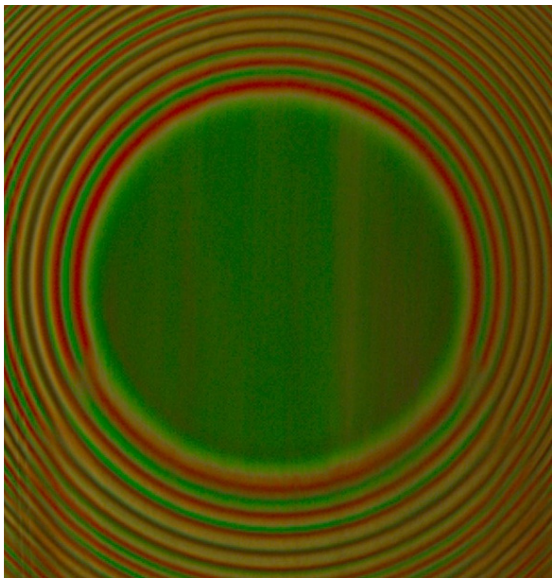


(**c**) R/G intensity profile of experimental image

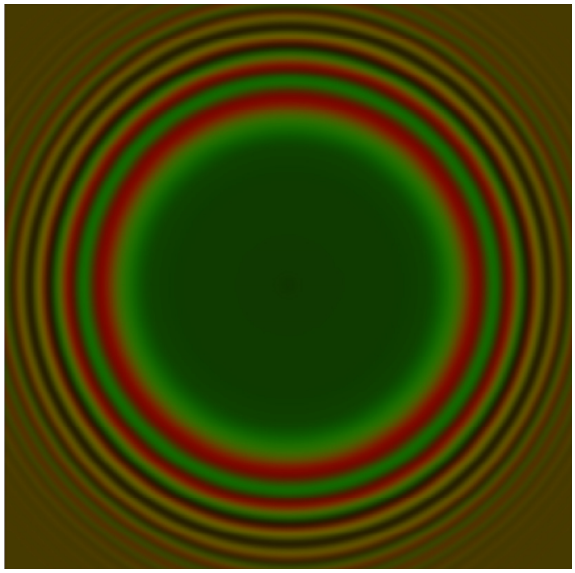


(**d**) R/G intensity profile of reconstructed image

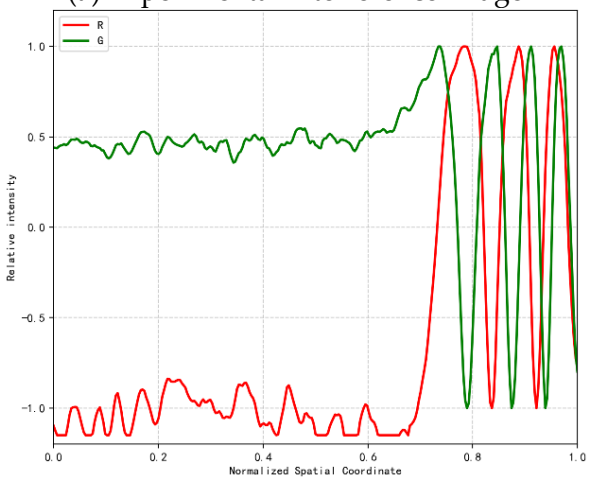
Figure 7. Interference response reconstruction at 200 mm/s operating condition.



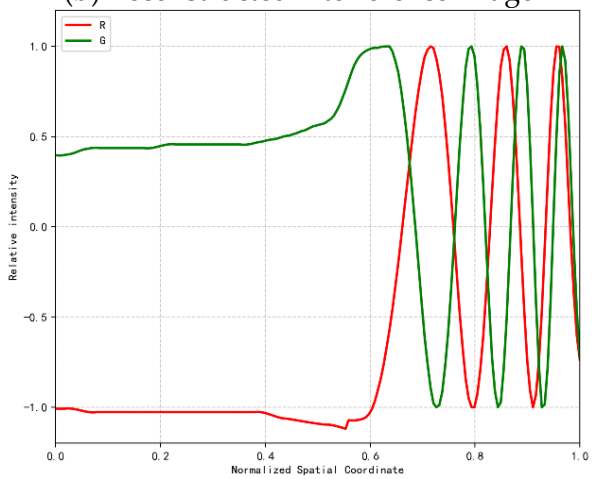
(**a**) Experimental interference image



(**b**) Reconstructed interference image

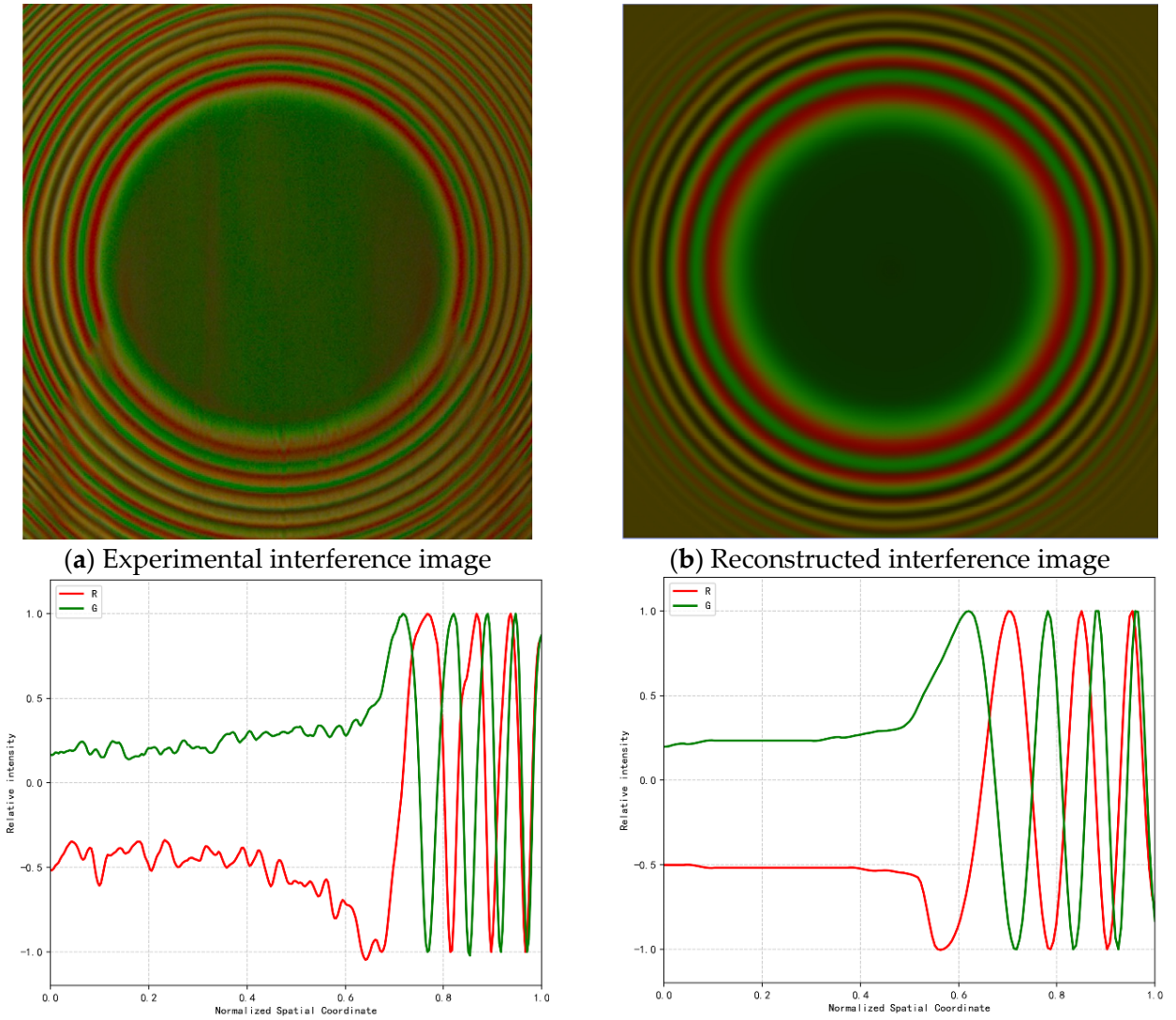


(**c**) R/G intensity profile of experimental image



(**d**) R/G intensity profile of reconstructed image

Figure 8. Interference response reconstruction at 105 mm/s operating condition.



(**a**) Experimental interference image (**b**) Reconstructed interference image

(**c**) R/G intensity profile of experimental image (**d**) R/G intensity profile of reconstructed image

Figure 9. Interference response reconstruction at 110 mm/s operating condition.

To further examine the consistency of the main interference characteristics between the experimental and reconstructed images, the relative R/G channel intensity profiles along the radial direction were extracted from both images. Since the experimental interference images were acquired under practical optical conditions, the original intensity profiles inevitably contain small fluctuations caused by camera noise, illumination variation, and optical instability. Therefore, the extracted profiles were normalized to facilitate the comparison of interference features among different cases. This normalization only adjusts the intensity scale of the profiles while preserving the relative spatial distribution characteristics of the interference features, without altering the characteristic fringe evolution. The R/G intensity profiles between the experimental and reconstructed images were compared under the same operating condition. The reconstructed profiles show comparable peak and valley locations and similar variation trends, fringe variation trends, and intensity gradient distributions with the experimental profiles. Furthermore, comparisons among different operating conditions reveal that both experimental and reconstructed images exhibit corresponding variations in the central flat-region intensity response and fringe distribution characteristics with changes in operating speed and lubrication state. The model preserves the differences in optical responses associated with different lubrication conditions, sup-

porting the consistency between the predicted film thickness and the corresponding optical interference characteristics.

For the validation conditions not involved in model training (105 and 110 mm/s), the reconstructed images still maintain the major interference structures and optical variation characteristics. Compared with the local random fluctuations observed in the experimental profiles, the reconstructed profiles exhibit smoother variation trends, suggesting that the model captures the stable characteristics of the interference response while reducing the influence of experimental disturbances.

4.4. Consistency Analysis of Predicted Film Thickness

To further examine the physical consistency of the proposed prediction framework, a closed-loop validation process was established. In this study, the purpose of interference-image reconstruction is not to achieve pixel-level reproduction of the experimentally acquired intensity distribution, but to preserve the optical response characteristics corresponding to the predicted representative film-thickness state. Specifically, the predicted film thickness h_{pred} was converted into a synthetic interference image I_{render} through the differentiable optical renderer. The generated image was subsequently re-input into the trained network to obtain a secondary prediction h_{recon}. The consistency error between h_{pred} and h_{recon} was calculated to quantify the deviation introduced during the forward–inverse transformation. As summarized in Table 4, the closed-loop consistency was evaluated under both known and independent validation conditions. For the known conditions, the consistency errors remained within 5%, indicating that the predicted film thickness could be stably maintained after optical rendering and re-prediction process. For the independent validation conditions, the deviation remained below 10%. These results demonstrate that the proposed framework preserves a consistent mapping relationship among operating conditions, film thickness states, and optical interference responses during the closed-loop transformation process.

Table 4. Comparison between predicted and re-predicted film thickness.

Speed (mm/s)	h_{pred} (nm)	h_{recon} (nm)	Consistency Error (%)
100	35.77	34.98	2.21
150	23.30	22.30	4.29
200	20.20	21.18	4.85
105	25.49	24.77	2.82
110	19.56	20.47	4.65

Compared with the initial prediction results in Table 3, the secondary prediction h_{recon} exhibits slightly larger deviations, which are attributed to the additional rendering and re-prediction process introduced in the closed-loop pathway. This deviation is consistent with the error accumulation characteristics of the forward–inverse transformation.

4.5. Comparison with Baseline and Ablation Analysis

To further evaluate the effectiveness of the proposed DW-PG-GNN framework, comparisons with a conventional interpolation method and an ablation baseline were conducted on the blind test speeds (105 mm/s and 110 mm/s). The cubic spline interpolation method was selected as a representative numerical interpolation approach, while the ablation baseline was constructed by removing the neural refinement and optical consistency constraints while retaining the basic physics-based prior. The comparison results are summarized in Table 5.

Table 5. Comparison of different methods for unseen entrainment-speed state prediction.

Method Category	Specific Approach	105 mm/s	110 mm/s	Mean Relative Error (%)
Numerical interpolation method	Cubic spline interpolation	33.40 nm	31.88 nm	50.41
Ablation baseline	Physics-based prior without refinement and optical constraints	28.28 nm	25.88 nm	24.26
Proposed framework	Full DW-PG-GNN	25.49 nm	19.56 nm	7.13

(Note: The ground-truth film thickness values are 27.00 nm and 18.00 nm for 105 mm/s and 110 mm/s, respectively.).

As shown in Table 5, the cubic spline interpolation method predicted film thicknesses of 33.40 nm and 31.88 nm at 105 mm/s and 110 mm/s, respectively, resulting in a mean relative error of 50.41%. This indicates that direct numerical interpolation based only on discrete speed–thickness relationships has limited capability for predicting unseen lubrication states under the investigated conditions.

The ablation baseline achieved a mean relative error of 24.26%, but its prediction accuracy was lower than that of the complete framework, particularly at 110 mm/s. In comparison, the complete DW-PG-GNN framework achieved a lower mean relative error of 7.13% by integrating neural refinement and optical consistency constraints. These results demonstrate the effectiveness of the proposed physics-guided framework for intermediate lubrication-state prediction from sparse experimental data.

4.6. Limitations and Practical Considerations

Although the proposed DW-PG-GNN framework demonstrates the feasibility of continuous lubrication-state learning from sparse dichromatic interference data, several limitations should be acknowledged. The integration of graph representation learning, implicit neural representation, differentiable optical rendering, and physics-guided optimization introduces additional computational complexity compared with conventional data-driven approaches. However, this increased computational burden mainly occurs during offline training, while the trained model can perform lubrication-state prediction through forward inference with reduced computational requirements compared with the training stage.

Similar to other deep learning-based frameworks, the proposed method may exhibit certain sensitivity to network initialization and hyperparameter selection. The introduced physical priors and consistency constraints provide additional regularization and help improve model stability, although further systematic investigations are still required. In addition, the present study focuses on controlled EHL conditions with entrainment speed as the only varying parameter. Therefore, further validation under broader operating conditions and optimization of computational efficiency are necessary to facilitate future deployment in real-time tribological monitoring applications.

5. Conclusions

To address the limitation of conventional dichromatic optical interferometry, which typically relies on discrete experimental measurements and therefore makes characterizing unseen intermediate lubrication states difficult, this study proposed a DW-PG-GNN framework for interpolation-based lubrication-state prediction from sparse discrete experimental data. Under fixed operating and material conditions, with entrainment speed treated as the only varying parameter, the proposed framework learned the interpolation relationship among entrainment speed, dichromatic interference images, and the average lubricant film thickness along the contact diameter, thereby enabling intermediate lubrication-state learning, dichromatic interference image reconstruction, and average lubricant film thickness prediction.

Comprehensive experimental validation under both known and independent validation operating conditions demonstrates that the proposed DW-PG-GNN framework achieves accurate average film-thickness prediction under the investigated conditions, reliable prediction capability for untrained entrainment-speed states, and physical consistency under controlled EHL conditions, thereby enabling interference-image reconstruction and average lubricant film thickness prediction at untrained operating conditions within the investigated range. The demonstrated interpolation capability is established under the present controlled parameter setting, while the effects of coupled variations in other EHL parameters remain to be further investigated.

Author Contributions: Conceptualization, X.Z.; methodology, P.Y. and X.Z.; software, J.W. and Z.S.; data curation, P.Y., J.W., Z.S. and C.H.; writing—original draft preparation, Z.S., C.H. and J.W.; writing—review and editing, X.Z. and P.Y.; supervision, X.Z. and Y.Z.; funding acquisition, P.Y. All authors have read and agreed to the published version of the manuscript.

Funding: This research is supported by the International Cooperation Project of Science and Technology of Henan (252102521092).

Data Availability Statement: The raw data supporting the conclusions of this article are available on request from the corresponding author. No publicly archived datasets were generated within this theoretical and numerical simulation research.

Conflicts of Interest: The authors declare no conflict of interest.

References

1. Hamrock, B.J.; Schmid, S.R.; Jacobson, B.O. *Fundamentals of Fluid Film Lubrication*; CRC Press: Boca Raton, FL, USA, 2004. [CrossRef]
2. Marian, M.; Bartz, M.; Wartzack, S.; Rosenkranz, A. Non-Dimensional Groups, Film Thickness Equations and Correction Factors for Elastohydrodynamic Lubrication: A Review. *Lubricants* **2020**, *8*, 95. [CrossRef]
3. Lugt, P.M.; Morales-Espejel, G.E. A Review of Elasto-Hydrodynamic Lubrication Theory. *Tribol. Trans.* **2011**, *54*, 470–496. [CrossRef]
4. Bair, S.; Habchi, W. Quantitative Elastohydrodynamic Lubrication—Seventeen Years In. *J. Tribol.* **2024**, *146*, 080801. [CrossRef]
5. Kumar, R.; Azam, M.S.; Ghosh, S.K.; Yadav, S. 70years of Elastohydrodynamic Lubrication (EHL): A Review on Experimental Techniques for Film Thickness and Pressure Measurement. *MAPAN* **2018**, *33*, 481–491. [CrossRef]
6. Gasni, D.; Wan Ibrahim, M.K.; Dwyer-Joyce, R.S. Measurements of lubricant film thickness in the iso-viscous elastohydrodynamic regime. *Tribol. Int.* **2011**, *44*, 933–944. [CrossRef]
7. Dou, P.; Jia, Y.; Zheng, P.; Wu, T.; Yu, M.; Reddyhoff, T.; Peng, Z. Review of ultrasonic-based technology for oil film thickness measurement in lubrication. *Tribol. Int.* **2022**, *165*, 107290. [CrossRef]
8. Glovnea, R.; Furtuna, M.D.; Nagata, Y.; Sugimura, J. Electrical Methods for the Evaluation of Lubrication in Elastohydrodynamic Contacts. *Tribol. Online* **2012**, *7*, 46–53. [CrossRef]
9. Chennaoui, M.; Fowell, M.; Liang, H.; Kadiric, A. A Novel Set-Up for In Situ Measurement and Mapping of Lubricant Film Thickness in a Model Rolling Bearing Using Interferometry and Ratiometric Fluorescence Imaging. *Tribol. Lett.* **2022**, *70*, 85. [CrossRef]
10. Liu, H.C.; Guo, F.; Guo, L.; Wong, P.L. A Dichromatic Interference Intensity Modulation Approach to Measurement of Lubricating Film Thickness. *Tribol. Lett.* **2015**, *58*, 15. [CrossRef]
11. Bai, Q.; Guo, F.; Wong, P.L.; Jiang, P. Online Measurement of Lubricating Film Thickness in Slider-on-Disc Contact Based on Dichromatic Optical Interferometry. *Tribol. Lett.* **2017**, *65*, 145. [CrossRef]
12. Tomota, T.; Tohyama, M.; Yagi, K. Elucidation of contact state on various rough surfaces via highly robust colorimetric optical interferometry. *Sci. Rep.* **2022**, *12*, 178. [CrossRef] [PubMed]
13. Ken, N.; Chiharu, T.; Satoru, M. Measurements of Lubricant Film Thickness by Optical Interference. *Hyomen Kagaku* **2017**, *38*, 111–116. [CrossRef]
14. MacLaren, A.; LaMascus, P.; Carpick, R.W. Enhancing the Range and Reliability of the Spacer Layer Imaging Method. *Tribol. Lett.* **2024**, *72*, 95. [CrossRef]
15. Josephine, K.; Volker, S.; Gerhard, P.; Max, M. Enhancing practical modeling: A neural network approach for locally-resolved prediction of elastohydrodynamic line contacts. *Tribol. Int.* **2024**, *199*, 109988. [CrossRef]

16. Sose, A.; Joshi, S.; Kunche, L.; Wang, F.; Deshmukh, S. A review of recent advances and applications of machine learning in tribology. *Phys. Chem. Chem. Phys.* **2023**, *25*, 4408–4443. [CrossRef] [PubMed]
17. Marian, M.; Mursak, J.; Bartz, M.; Profito, F.J.; Rosenkranz, A.; Wartzack, S. Predicting EHL film thickness parameters by machine learning approaches. *Friction* **2023**, *11*, 992–1013. [CrossRef]
18. Issa, J.; El Hajj, A.; Vergne, P.; Habchi, W. Machine Learning for Film Thickness Prediction in Elastohydrodynamic Lubricated Elliptical Contacts. *Lubricants* **2023**, *11*, 497. [CrossRef]
19. Marian, M.; Tremmel, S. Current Trends and Applications of Machine Learning in Tribology—A Review. *Lubricants* **2021**, *9*, 86. [CrossRef]
20. Kipf, T.; Welling, M. Semi-Supervised Classification with Graph Convolutional Networks. *arXiv* **2016**, arXiv:1609.02907. [CrossRef]
21. Sitzmann, V.; Martel, J.N.P.; Bergman, A.W.; Lindell, D.B.; Wetzstein, G. Implicit Neural Representations with Periodic Activation Functions. *arXiv* **2020**, arXiv:2006.09661. [CrossRef]
22. Raissi, M.; Perdikaris, P.; Karniadakis, G.E. Physics-informed neural networks: A deep learning framework for solving forward and inverse problems involving nonlinear partial differential equations. *J. Comput. Phys.* **2019**, *378*, 686–707. [CrossRef]
23. Rui, W.; Rose, Y. Physics-Guided Deep Learning for Dynamical Systems: A Survey. *ACM Comput. Surv.* **2021**, *58*, 1–31. [CrossRef]
24. Born, M.; Wolf, E.; Hecht, E. Principles of Optics: Electromagnetic Theory of Propagation, Interference and Diffraction of Light. *Phys. Today* **2000**, *53*, 77. [CrossRef]
25. Johnston, G.J.; Wayte, R.; Spikes, H.A. The Measurement and Study of Very Thin Lubricant Films in Concentrated Contacts. *Tribol. Trans.* **1991**, *34*, 187–194. [CrossRef]

Disclaimer/Publisher's Note: The statements, opinions and data contained in all publications are solely those of the individual author(s) and contributor(s) and not of MDPI and/or the editor(s). MDPI and/or the editor(s) disclaim responsibility for any injury to people or property resulting from any ideas, methods, instructions or products referred to in the content.